Monthly Notices of the ROYAL ASTRONOMICAL SOCIETY

MNRAS **524,** 2064–2077 (2023)
Advance Access publication 2023 June 24

https://doi.org/10.1093/mnras/stad1839

A subarcsec localized fast radio burst with a significant host galaxy dispersion measure contribution

M. Caleb [1,2,3★] L. N. Driessen [1,4] A. C. Gordon,[5] N. Tejos [6] L. Bernales,[6] H. Qiu [7] J. O. Chibueze [8,9,10] B. W. Stappers [2] K. M. Rajwade [2,11] F. Cavallaro,[12,13] Y. Wang [1,14,15] P. Kumar [16,17] W. A. Majid,[18,19] R. S. Wharton,[18] C. J. Naudet,[18] M. C. Bezuidenhout,[8] F. Jankowski [2,20] M. Malenta,[2] V. Morello [2] S. Sanidas,[2] M. P. Surnis [2,21] E. D. Barr,[22] W. Chen [22] M. Kramer,[2,22] W. Fong,[5] C. D. Kilpatrick [5] J. Xavier Prochaska,[23,24] S. Simha,[23] C. Venter,[8] I. Heywood [25,26] A. Kundu [8] and F. Schussler[27]

Affiliations are listed at the end of the paper

Accepted 2023 June 9. Received 2023 June 9; in original form 2023 February 17

ABSTRACT

We present the discovery of FRB 20210410D with the MeerKAT radio interferometer in South Africa, as part of the MeerTRAP commensal project. FRB 20210410D has a dispersion measure DM = 578.78 ± 2 pc cm^{-3} and was localized to subarcsec precision in the 2 s images made from the correlation data products. The localization enabled the association of the FRB with an optical galaxy at $z = 0.1415$, which when combined with the DM places it above the 3σ scatter of the Macquart relation. We attribute the excess DM to the host galaxy after accounting for contributions from the Milky Way's interstellar medium and halo, and the combined effects of the intergalactic medium and intervening galaxies. This is the first FRB that is not associated with a dwarf galaxy to exhibit a likely large host galaxy DM contribution. We do not detect any continuum radio emission at the FRB position or from the host galaxy down to a 3σ rms of 14.4 μJy beam^{-1}. The FRB has a scattering delay of $29.4^{+2.8}_{-2.7}$ ms at 1 GHz, and exhibits candidate subpulses in the spectrum, which hint at the possibility of it being a repeating FRB. Although not constraining, we note that this FRB has not been seen to repeat in 7.28 h at 1.3 GHz with MeerKAT, 3 h at 2.4 GHz with Murriyang, and 5.7 h at simultaneous 2.3 GHz and 8.4 GHz observations with the Deep Space Network. We encourage further follow-up to establish a possible repeating nature.

Key words: stars: neutron – radio continuum: transients.

1 INTRODUCTION

Fast radio bursts (FRBs) are energetic bursts of radio emission spread over luminosity distances ranging from 131 Mpc (Kirsten et al. 2022) to 6 Gpc (Ryder et al. 2022). FRBs typically last a few microseconds to milliseconds in duration with luminosities spanning 10^{38}–10^{46} erg s^{-1} (Luo et al. 2020). Their 10^{12} times higher luminosities compared to pulsars and rotating radio transients (assuming beamed radiation) suggest extreme neutron star manifestations as progenitors, which could be isolated, or involve interaction or collision. Other progenitor models involving black holes, white dwarfs, and even exotic stars have also been proposed. Synchrotron-maser emission produced at the shock front between a pulsar wind nebula and a supernova remnant or the interstellar medium (ISM), as well as giant flares from within the magnetosphere of the neutron star, are popular progenitor models (Platts et al. 2019). Repeating FRBs have been observed to emit at frequencies from 110 MHz (Pleunis et al. 2021a) all the way up to 8 GHz (Gajjar et al. 2018), whereas apparently non-repeating sources have only been detected from 350 MHz (Parent et al. 2020) up to 1.4 GHz. However, their emission outside this frequency range remains uncertain despite attempts to detect them beyond these frequencies.

In the current known sample, 1 in every 14 FRBs have been observed to repeat and whether they all do is very much an open question (e.g. Caleb, Spitler & Stappers 2018). Both repeating and (as-yet) non-repeating ones are slowly and steadily being localized to (sub)arcsec precision either through their repeat pulses or interferometric localizations upon detection (e.g. Chatterjee et al. 2017; Bannister et al. 2019). Optical observations of the well-localized ones have resulted in a sample of 24 FRBs with secure host galaxy associations with redshifts in the range $z = 0.03$–1.02 (Ryder et al. 2022; Gordon et al. 2023). Presently, the global host galaxy demographics are diverse to say the least. FRBs are seen to arise in starburst to nearly quiescent galaxies and are typically not associated with the nuclei of the hosts (Bhandari et al. 2022b). Positional offsets from the centres of the host galaxies range from 0.8 to 20.1 kpc, with the latter being an FRB that resides in a globular cluster in the M81 system (Bhandari et al. 2022b). A handful of galaxy images at high spatial resolution show the FRBs to be residing in the spiral arms of galaxies (Mannings et al. 2021). A sample of nine FRB host galaxies with redshifts below 0.5 asserts a strong correlation between the rotation measures (RMs) of the host galaxies and the estimated host dispersion measure (DM) contributions (Mannings et al. 2022). The

★ E-mail: manisha.caleb@sydney.edu.au

© 2023 The Author(s)
Published by Oxford University Press on behalf of Royal Astronomical Society

Downloaded from https://academic.oup.com/mnras/article/524/2/2064/7207412 by Univ. of California, Santa Cruz user on 21 July 2023

magnetic fields ($\approx 0.5\,\mu$G) of the sample in Mannings et al. (2022) are weaker than those characteristic of the Solar neighbourhood ($\approx 6\,\mu$G). However, they are relatively consistent with a lower limit on the observed range of $2-6\,\mu$G for star-forming, disc galaxies.

Overall, there is no clear distinction between the hosts of repeating and non-repeating FRBs. However, a couple of prolific FRBs, FRBs 20121102A and 20190520B are seen to reside in dwarf galaxies and are associated with persistent emission on compact spatial scales (Marcote et al. 2017; Niu et al. 2022). These two FRBs are observed to exhibit temporal RM variations indicative of magnetic fields varying on short time-scales, which may correlate with the presence of persistent emission. Furthermore, both these FRBs exhibit significant host galaxy DM contributions (Tendulkar et al. 2017; Niu et al. 2022) which are expected to arise from the vicinities of the progenitors and are attributed to the likely dense persistent radio sources (PRSs) associated with them. Rafiei-Ravandi et al. (2021) have found statistical evidence for a population of FRBs discovered with CHIME at $z \sim 0.4$ with host galaxy DM contributions of $\sim 400\,\mathrm{pc\,cm^{-3}}$. This may be plausible by some halo gas models (Rafiei-Ravandi et al. 2021), as well as augmentation by intervening foreground galaxies (James et al. 2022a). Host galaxies belonging to massive galaxy clusters have also been seen to contribute to the observed excess extragalactic DMs of two FRB sources (Connor et al. 2023).

More recently, FRB 20210117A discovered by the ASKAP telescope was found to have host galaxy characteristics similar to those of FRBs 20121102A and 20190520B and an excess DM contribution from the host (Bhandari et al. 2022a). However, the FRB has not yet been observed to repeat in 9.2 h of radio follow-up. While there is no direct evidence of *any* FRB being a true non-repeater, such as being produced from a cataclysmic event, the analysis of a large sample of repeaters and non-repeaters by Pleunis et al. (2021b) has shown clear distinctions in the pulse morphology between the two classes. Pleunis et al. (2021b) show that an FRB can be probabilistically classified as either a one-time event or a repeater burst, based solely on its burst morphology. Bursts from repeating sources, on average, have larger widths and, on average are spectrally band-limited (i.e. narrower in bandwidth). These features can be related to the presence of downward frequency drifting or the 'sad-trombone' effect, where subbursts under the FRB pulse envelope are seen to cascade downward towards lower frequencies at later times (Hessels et al. 2019). This behaviour is observed in almost all repeating FRBs and is likely a combination of the unknown emission mechanism and line-of-sight propagation effects. Based on the known sample of repeating and non-repeating FRBs, it appears that frequency downward-drifting may be predictive of repetition. In some cases, various subpulses of the same FRB are even observed to have slightly different DMs (Day et al. 2020).

In this paper, we present the discovery of FRB 20210410D, which bears some of the hallmarks of repeating FRBs, but has not yet been observed to repeat in follow-up radio observations. In Section 2, we present the observational configuration of the MeerKAT telescope and the details of the transient detection pipeline used by the MeerTRAP project. Section 3 reports the discovery and the measured and inferred properties of the FRB. We present our analyses and results in Section 4 and discuss them in Section 5. A summary and our conclusions are presented in Section 6.

2 THE MEERTRAP PROJECT

The MeerKAT radio telescope is a 64-dish interferometer operated by the South African Radio Astronomy Observatory (SARAO) in the Karoo region in South Africa. The dishes are spread over 8 km, with 40 of them concentrated in the inner ∼1-km core. Each telescope is 13.5-m in diameter and currently operates regularly in the *L* band (856–1712 MHz) and the *UHF* band (544–1088 MHz). The MeerTRAP project is a complementary programme to search for pulsars and fast transients while piggybacking on the large survey programmes of MeerKAT. MeerKAT simultaneously observes in incoherent and coherent modes using the MeerTRAP backend. The MeerTRAP backend is the association of two systems: the Filterbank and Beamforming User Supplied Equipment (FBFUSE), a many-beam beamformer that was designed and developed at the Max-Planck-Institut für Radioastronomie in Bonn (Barr 2018; Chen et al. 2021), and the Transient User Supplied Equipment (TUSE), a real-time transient detection instrument developed by the MeerTRAP team at the University of Manchester. When operating at *L* band in the coherent mode, the voltages from the inner 40 dishes of the ∼1-km core of the array are coherently combined to form up to 780 beams on the sky with an aggregate field of view (FoV) of $\sim 0.4\,\mathrm{deg^2}$ (i.e. overlap at 25 per cent of the peak power). In the incoherent mode, the intensities of all available MeerKAT dishes (up to a maximum of 64) are added to create a less sensitive but much wider FoV of $\sim 1.3\,\mathrm{deg^2}$ (Rajwade et al. 2021). We utilize the highly optimized Graphics Processing Unit (GPU)-based ASTROACCELERATE software (Armour et al. 2012; Adámek & Armour 2020) to search for dispersed signals. In the *L* band, the real-time search is performed by incoherently de-dispersing in the DM range 0–5118.4 $\mathrm{pc\,cm^{-3}}$ and searching up to maximum boxcar widths of 0.67 s. The extracted candidate files contain raw filterbank data of the dispersed pulse and additional padding of 0.5 s at the start and at the end of the file. See Caleb et al. (2022), Rajwade et al. (2022), and Jankowski, Bezuidenhout & et al. (2023) for more details. Additionally, correlated visibilities from as many dishes as are available are recorded during each observation to search for and identify serendipitous transients in images of the field.

3 DISCOVERY

FRB 20210410D shown in Fig. 1 was discovered while commensally observing with a MeerKAT open-time proposal (SCI-20210212-CV-01; PI Venter) to identify persistent radio emission associated with well-localized FRBs (Chibueze et al. 2022). It was detected by the MeerTRAP real-time transient pipeline in the incoherent beam while observing the position of FRB 20190611B. In offline analysis, we optimized the signal-to-noise (S/N) ratio of FRB 20210410D to ∼42 for a DM of $578.78\,\mathrm{pc\,cm^{-3}}$ and width of 26.6 ms. See Table 1 for more details. As the FRB was detected in the incoherent beam, it could lie anywhere within $\sim 1.3\,\mathrm{deg^2}$. However, since it was bright, we were able to localize it to (sub)arcsec precision in the simultaneous shortest time-scale correlated visibilities. See Section 4.2.1 for details.

4 ANALYSIS

4.1 Beamformed radio data analysis

4.1.1 DM estimation

The relatively wide width of FRB 20210410D suggests a repeater origin (Pleunis et al. 2021b). Consequently, we calculated the DM to optimize the structure under the burst envelope using `DM_phase` (https://github.com/danielemichilli/DM_phase). The `DM_phase` algorithm finds the structure-optimized DM of a burst by maximizing

Downloaded from https://academic.oup.com/mnras/article/524/2/2064/7207412 by Univ. of California, Santa Cruz user on 21 July 2023

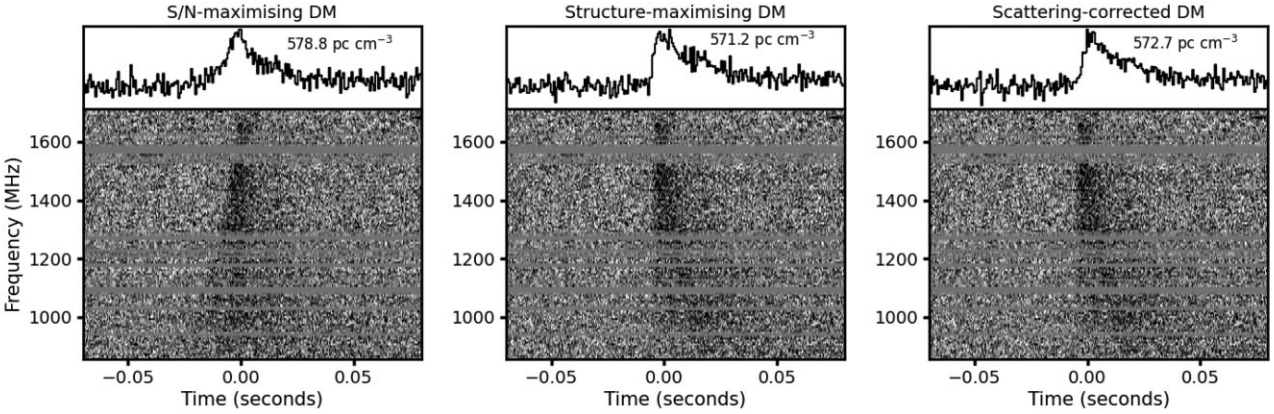

Figure 1. Dynamic spectra of the FRB dedispersed to the S/N-maximizing DM (left-hand panel), structure-maximizing DM (middle panel), and scattering-corrected DM. The top panel of each case shows the frequency-averaged pulse profile. The data are uncalibrated and the flux densities are in arbitrary units.

Table 1. Observed and inferred properties of FRB 20210410D and the associated host galaxy.

Parameter	Unit	FRB 20210410
	Measured	
$\mathrm{MJD}^{a}_{\mathrm{topo}}$		59314.4673892632
$\mathrm{UTC}^{a}_{\mathrm{topo}}$		2021-04-10 11:13:02.432
Beam		Incoherent beam
RA	(hms)	$21^{\mathrm{h}}44^{\mathrm{m}}20\overset{\mathrm{s}}{.}7\mathrm{s} \pm 0\overset{''}{.}8$
Dec.	(dms)	$-79^{\circ}19'05\overset{''}{.}5 \pm 0\overset{''}{.}5.$
l	(deg)	312.3222099
b	(deg)	−34.1293941
S/N-maximizing DM	(pc cm^{-3})	578.78 ± 2.0
Structure-maximizing DM	(pc cm^{-3})	571.16 ± 0.97
Scattering-corrected DM	(pc cm^{-3})	572.65 ± 0.38
S/N		42
Scattering time, τ_{s} at 1 GHz	(ms)	$29.4^{+2.8}_{-2.7}$
	Inferred	
$S^{\mathrm{b}}_{\mathrm{peak}}$	(Jy)	1.5
F^{b}	(Jy ms)	35.4
$\mathrm{DM}_{\mathrm{MW,\ NE2001}}$	(pc cm^{-3})	56.2
$\mathrm{DM}_{\mathrm{MW,\ YMW16}}$	(pc cm^{-3})	42.2
$\mathrm{DM}_{\mathrm{halo}}$	(pc cm^{-3})	40
$\mathrm{DM}_{\mathrm{EG}}$	(pc cm^{-3})	489
	Host galaxy	
Host galaxy name		J214420.69−791904.8
Redshift (z)		0.1415
g	(AB mag)	21.77 ± 0.05
r	(AB mag)	20.65 ± 0.03
i	(AB mag)	20.10 ± 0.02
z	(AB mag)	20.23 ± 0.04
Y	(AB mag)	19.76 ± 0.16
J	(AB mag)	20.02 ± 0.21
Stellar metallicity	$\log\,(Z_*/\mathrm{Z}_{\odot})$	$-1.08^{+0.21}_{-0.33}$
Stellar mass	$\log\,(M_*/\mathrm{M}_{\odot})$	$9.46^{+0.05}_{-0.06}$
0–100 Myr integrated SFR	($\mathrm{M}_{\odot}$ yr^{-1})	$0.03^{+0.03}_{-0.061}$
Projected offset from galaxy centre	(kpc)	2.9
Hα flux density	(erg s^{-1} cm^{-2})	1.5×10^{-16}

Note. [a]Topocentric arrival times measured at the highest frequency channel, 1711.58 MHz.

Downloaded from https://academic.oup.com/mnras/article/524/2/2064/7207412 by Univ. of California, Santa Cruz user on 21 July 2023

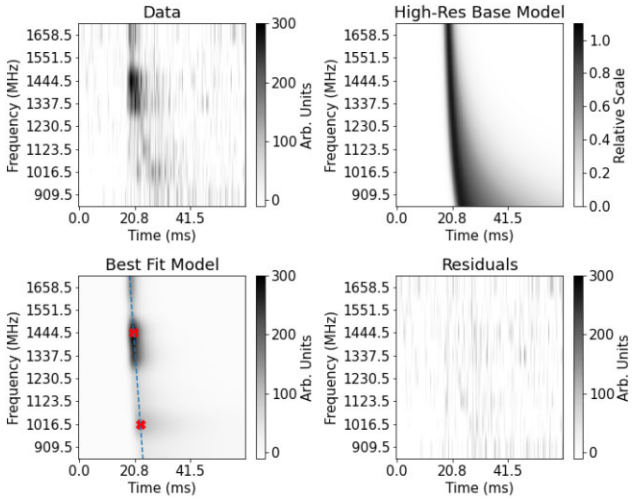

Figure 2. Multifrequency modelling of the pulse profile dedispersed to the structure-maximizing DM. We transform the pulse profile into eight subbands and apply an eight subband multifrequency scattering single pulse model to fit the data. Our results show that a shifted scattering model best describes the pulse profile of FRB 20210410D. The two candidate subpulse positions are marked in the best-fitting model as crosses, with the measured drift rate drawn as the dashed line. We display the data, best-fitting model, and residuals for comparison.

the coherent power across the bandwidth (Seymour, Michilli & Pleunis 2019). We dedispersed the data over a trial DM range of 565.0 pc cm^{-3} $\leq$ DM $\leq$ 580.0 pc cm^{-3} in steps of 0.1 pc cm^{-3}. The uncertainty on each DM estimate was calculated by converting the standard deviation of the coherent power spectrum into a standard deviation in DM via the Taylor series. We measure a structure-optimized DM of 571.2 $\pm$ 1 pc cm^{-3} for FRB 20210410D. Visual inspection of the spectrum after dedispersing to the structure-optimized DM showed hints of scattering.

4.1.2 Scattering analysis

We performed a 2D scattering fit to the FRB using a PYTHON-based burst model software and Monte Carlo sampling methodology based on Qiu et al. (2020). We utilize a robust dynamic modelling in a higher resolution model to account for the convolved scatter broadening, dispersion smearing, and intrinsic pulse width. The model also takes into account of any possible varying pulse arrival time across frequency due to incomplete dedispersion as seen in Hessels et al. (2019). For FRB 20210410D, we assume a single Gaussian pulse model with scatter broadening. To avoid confusion with intrinsic pulse width and also to accurately determine scattering caused by inhomogeneous plasma, we fix the scattering index to $\alpha = -4$.

We measure a scattering time of $29.4^{+2.8}_{-2.7}$ ms at 1 GHz and an intrinsic pulse width of $1\sigma = 2.0 \pm 0.3$ ms. The pulse position is delayed in relation to frequency when structure maximized. This can be characterized as an excess dispersion delay of $1.8^{+0.5}_{-0.4}$ pc cm^{-3}, which corresponds to the scattering corrected DM. The pulse position shift can also be characterized by a drift rate of 1.2 ± 0.4 ms/107 MHz by measuring the two subband positions at 1444.5 and 1016.5 MHz. Our relatively coarse time resolution of 306.24 µs does not allow us to robustly distinguish between the two. We show our best-fitting model and residuals in Fig. 2 and the parameter posteriors in Fig. 3.

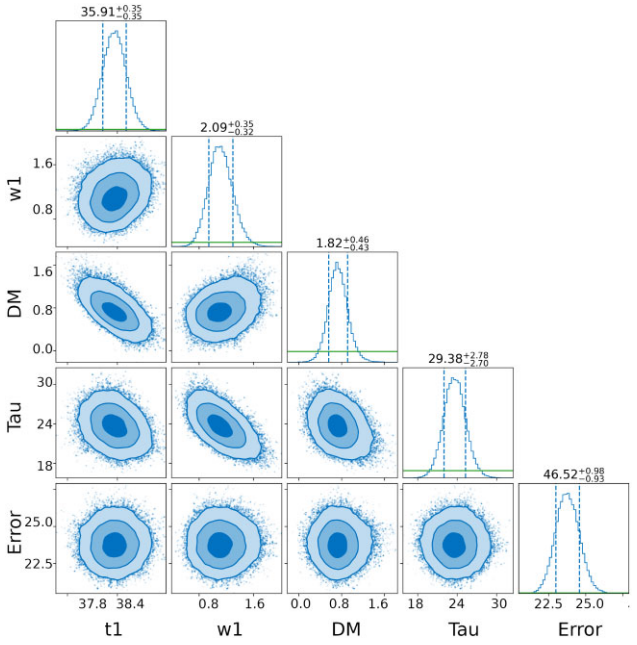

Figure 3. The posterior for modelling the burst dynamic spectrum. We display the key parameters: pulse position (t1), intrinsic width (w1), excess DM (DM), and scattering (τ). The three shades of contour correspond to 1σ, 2σ, and 3σ confidence levels.

4.2 Imaging radio data analysis

4.2.1 FRB 20210410D localization

The shortest integration image we could make during the 2021 April 10 observation when FRB 20210410D was detected was 2 s. Although the standard integration time for MeerKAT imaging data is 8 s, it is possible to go to shorter integration times for certain projects. The MeerKAT open-time proposal SCI-20210212-CV-01 used an integration time of 2 s for their data, as there was a possibility of detecting repeat pulses from the target FRB 20190611B. As such, we imaged the observations into 2 s chunks. The 2 s images have a typical root-mean-square (rms) noise of ∼0.7 mJy beam^{-1} and a synthesized beam size of 21 arcsec × 10 arcsec.

To find the position of the FRB we used difference imaging. The total dispersion delay of FRB 20210410D across the MeerKAT band is ∼2.4 s and based on the time of detection, we expect most of the FRB to lie within a single 2 s image. We use `WSClean` to produce 20 × 2 s images around the time of the MeerTRAP FRB detection. We then combined these images into an average image and subtracted this average image from each individual 2 s image. The subtracted images of the time-step before, the time-step of, and the time-step after the FRB detection are shown in Fig. 4. We can see in this figure that only the difference image at the time of the detection has a bright-spot, which is ∼40 arcmin from the phase centre of the images. As this source in the difference image is detected at the time that we expect to see the FRB, it is outside of the MeerTRAP coherent beam tiling as expected, it is the only source in the difference image, and there is no source in the difference images surrounding the expected FRB detection time, we determine that this source is the FRB. The FRB has a flux density of 35 mJy with a ∼1.8 mJy rms.

The position of the FRB detected in the difference image prior to astrometric correction is $21^{\rm h}44^{\rm m}20\overset{\rm s}{.}6 \pm 0\overset{''}{.}7 - 79^\circ19'04\overset{''}{.}8 \pm 0\overset{''}{.}3$.

Downloaded from https://academic.oup.com/mnras/article/524/2/2064/7207412 by Univ. of California, Santa Cruz user on 21 July 2023

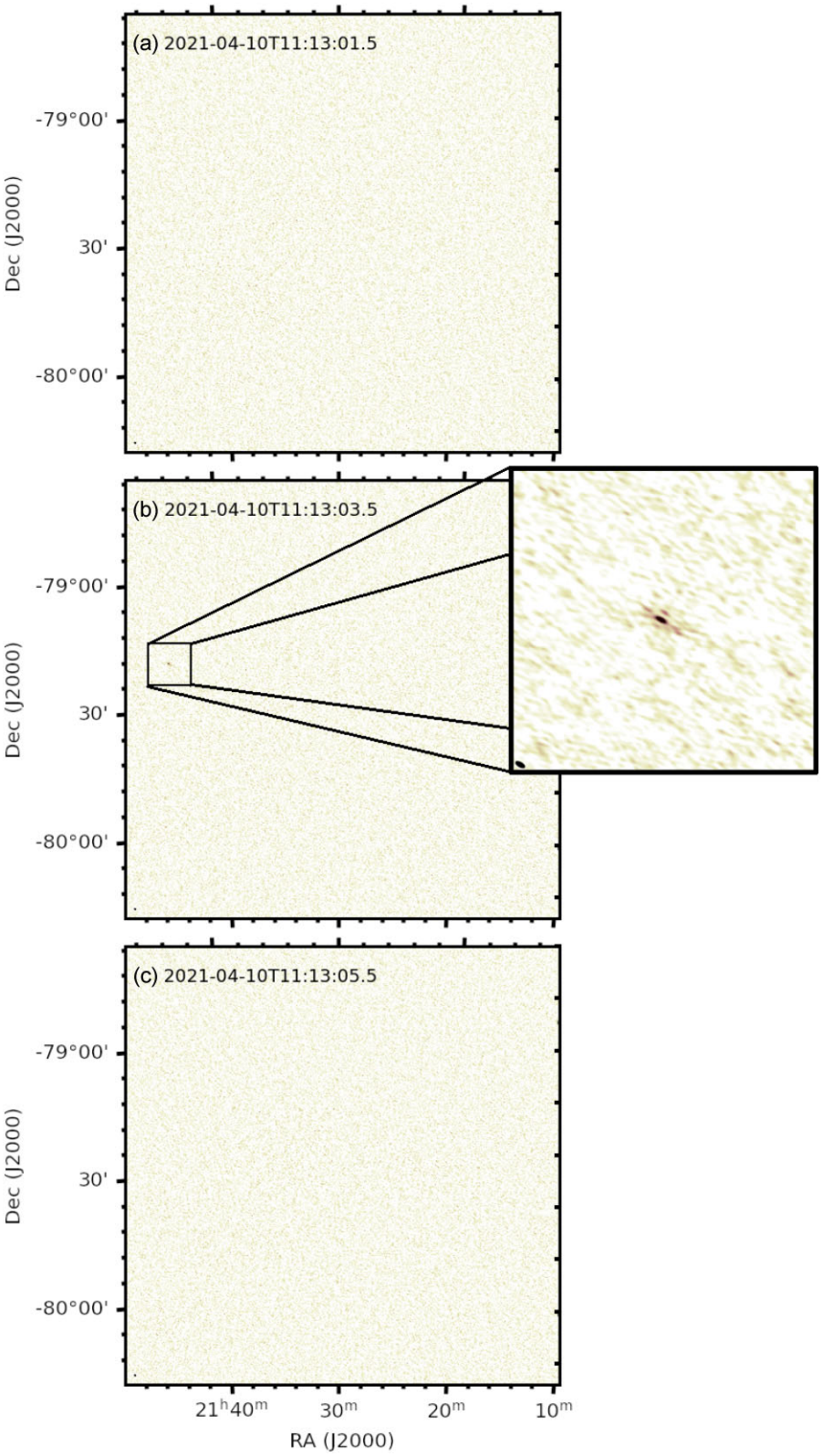

Figure 4. Difference images of (a) the time-step before, (b) the time-step of, and (c) the time-step after the FRB detection. The time-steps shown are the centre of the time slice. The colour scale is the same in each panel and the synthesized beam is shown in the bottom left corner of each panel and the inset image. The inset image shows a 1 arcmin × 1arcmin zoom in of the FRB position. No other variables are detected in this field in these time-steps.

Downloaded from https://academic.oup.com/mnras/article/524/2/2064/7207412 by Univ. of California, Santa Cruz user on 21 July 2023

Table 2. Coordinates of the ATPMN sources used as reference sources for the astrometric corrections. Only unresolved sources were used for the astrometry. Some ATPMN sources were not within the 2021 April 10 observation FoV but were within the 2021 September 05 observation FoV. The offsets are the separations between the ATPMN and MeerKAT positions before and after applying the astrometric corrections.

		2021 Apr 10 offset		2021 Sep 05 offset	
RA	Dec.	Before correction	After correction	Before correction	After correction
$20^h57^m06^s.5$	$-80°18'24''.3$	$1''.3$	$0''.84$	$0''.96$	$0''.17$
$20^h57^m06^s.5$	$-80°18'24''.3$			$1''.5$	$0''.51$
$21^h05^m45^s.0$	$-78°25'34''.5$	$1''.9$	$0''.87$	$1''.0$	$0''.2$
$21^h21^m40^s.8$	$-78°03'46''.7$	$1''.3$	$0''.49$	$0''.94$	$0''.44$
$21^h24^m40^s.9$	$-80°05'01''.0$	$0''.83$	$0''.64$	$0''.25$	$0''.5$
$21^h24^m40^s.9$	$-80°05'01''.0$			$0''.96$	$0''.41$
$21^h46^m30^s.0$	$-77°55'54''.7$	$1''.3$	$0''.69$	$1''.6$	$0''.8$
$21^h47^m05^s.8$	$-78°12'21''.9$	$0''.73$	$0''.24$	$0''.63$	$0''.15$
$21^h49^m30^s.7$	$-80°46'02''.5$	$1''.5$	$1''.0$	$0''.4$	$0''.11$
$21^h52^m03^s.2$	$-78°07'06''.4$	$0''.58$	$0''.21$	$0''.49$	$0''.39$
$21^h56^m47^s.8$	$-79°37'39''.1$	$0''.97$	$0''.58$	$0''.35$	$0''.2$
$21^h59^m01^s.2$	$-80°39'16''.8$	$1''.8$	$1''.6$	$0''.46$	$0''.13$
$21^h59^m16^s.6$	$-80°41'43''.8$	$1''.5$	$0''.88$	$0''.6$	$0''.54$
$22^h06^m11^s.2$	$-79°35'11''.8$	$1''.7$	$1''.2$	$0''.4$	$0''.19$

4.2.2 *Absolute astrometry*

We corrected the astrometry in the MeerKAT images using the method described in Driessen et al. (2022). We imaged the full-time integration image of 2.25 h to determine the astrometric correction. We first find the positions of the sources in the images using the Python Blob Detector and Source Finder[1] (PYBDSF). We then find Australian Telescope Compact Array (ATCA) Parkes-MIT-NRAO (PMN) (ATPMN; McConnell et al. 2012) sources within the MeerKAT FoV, excluding any sources that appear resolved in the MeerKAT images. There are 27 ATPMN sources in the FoV, 13 of which are resolved. The ATPMN positions of the unresolved sources, and the separations between the ATPMN and MeerKAT sources before and after applying the astrometric correction are shown in Table 2. The ATPMN survey has a median absolute astrometric uncertainty of $0''.4$ in both right ascension (RA) and declination (Dec). We use the matching ATPMN and MeerKAT point sources to solve for a transformation matrix to shift and rotate the MeerKAT sources to match the ATPMN source positions.[2] We apply the transformation matrix to all MeerKAT source positions and we combine the PYBDSF uncertainties and $0''.4$ ATPMN uncertainty in quadrature. In shorter time-scale MeerKAT imaging, 2 or 8 s images, we often do not detect many ATPMN sources. As such, we determine the astrometric correction using the sources extracted from the full integration image of the epoch and apply that correction to the sources extracted from the 2 or 8 s images. We find that the corrected position of the FRB is $21^h44^m20^s.7s \pm 0''.8 - 79°19'05''.5 \pm 0''.5$.

4.2.3 *Continuum source localization*

The FRB was detected in the ∼1-h long observation on 2021 April 10, ∼40 arcmin from the phase centre. This means that the sensitivity to faint, persistent emission near the FRB was low. A 3-h long observation on 2021 September 05 was pointed to accommodate three FRBs within the MeerKAT FoV. This meant that the position of FRB 20210410D was ∼28 arcmin from the phase centre resulting in higher sensitivity at the FRB position than in the detection observation. On 2021 September 05, a faint, $\sim 8\sigma$ (rms $= \sim 4.8\,\mu$Jy) persistent continuum source was detected ∼3 arcsec from the FRB position. We corrected the astrometry of the image (the offsets between the MeerKAT positions and ATPMN positions before and after correction are shown in Table 2) and found the corrected position of the persistent continuum source to be $21^h44^m19^s.5s \pm 0''.6 - 79°19'05''.8s \pm 0''.5$ (uncorrected: $21^h44^m19^s.4s \pm 0''.4 - 79°19'05''.4s \pm 0''.3$). The separation between the corrected FRB position and the corrected persistent continuum source position is $3''.3$. The MeerKAT persistent continuum source is consistent with the position of the galaxy at $z \sim 0.4$ (see Section 4.5 for details) as shown in Fig. 5 and is not a compact PRS as observed in a couple of repeating FRBs.

4.2.4 *Polarization analysis*

The FRB discovery was made while commensally observing with a MeerKAT open-time proposal that did not require polarization information. Consequently, a standard polarization calibrator was not observed. To extract the polarization information we used, in the 2 s image containing the FRB detection, J1619−8418 as the secondary and polarization calibrator. It is a known calibrator with very low linear (∼ 0.4 per cent) and circular (∼ 0.03 per cent) polarization.[3] We mapped Stokes Q, U, and V along with Stokes I using the IDIA pipeline.[4] FRB 20210410D was only detected in Stokes I and not in Stokes Q, U, or V, giving us a 3σ upper limit of about 18 per cent for each of them. We used the `RMsynth3D` algorithm from the RM-TOOLS[5] package to perform 3D RM synthesis on the image-frequency cube. The method transforms polarized intensity as a function of λ^2 to Faraday depth, ϕ, representing polarized intensity for different trial RMs in the range $[-150\,000, +150\,000]$. We did not detect a peak in the maximum polarized intensity map at the position of the

[1] https://www.astron.nl/citt/pybdsf/

[2] The code for performing the astrometric corrections can be found on GitHub: https://github.com/AstroLaura/MeerKAT_Source_Matching.

[3] https://archive-gw-1.kat.ac.za/public/meerkat/MeerKAT-L-band-Polarimetric-Calibration.pdf

[4] https://idia-pipelines.github.io/

[5] https://github.com/CIRADA-Tools/RM-Tools

Downloaded from https://academic.oup.com/mnras/article/524/2/2064/7207412 by Univ. of California, Santa Cruz user on 21 July 2023

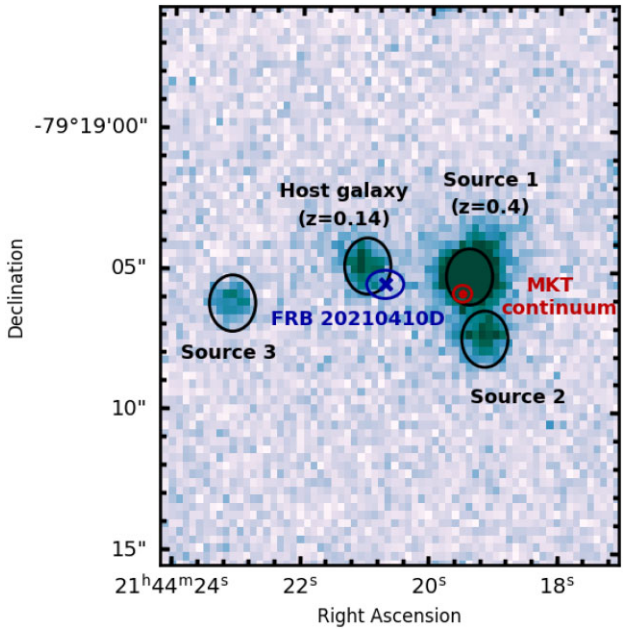

Figure 5. 200 s *r*-band exposure using the Goodman High Throughput Spectrograph (GHTS) on the SOAR 4.1 m telescope. The blue cross and ellipse represent the position of the FRB and the 2σ total uncertainty in the position. The red circle and ellipse represent the position of the continuum detection in the deep MeerKAT image and the 2σ total uncertainty in the position (see Section 4.2.3). Black circles are 1 arcsec in diameter and highlight other sources in the field. The absence of emission lines for sources 2 and 3 prevented an estimate of their redshifts.

FRB. We do, however, detect a peak at a 6σ significance with an RM of $-77\,929$ rad m^{-2}. This peak is not associated with any of the sources detected in the field in Fig. 5. Therefore, we consider this a spurious detection.

4.3 Radio follow-up for repeat bursts

4.3.1 MeerKAT

FRB 20210410D is approximately 1° away from the position of FRB 20190611B and 0.7° away from FRB 20190102C, both of which were observed as part of the open-time proposal with MeerKAT. The MeerTRAP backend was used to piggy-back these imaging observations to look for any repeat bursts from FRB 20190611B, FRB 20190102C, and, consequently, from FRB 20210410D in real-time. No other radio bursts (whether repeat bursts from the known FRBs in the field or completely unassociated) were detected in our beamformed data down to a fluence limit of 0.09 Jy ms in a total of 7.28 h of time spent on the FRB source with MeerKAT.

4.3.2 Murriyang

In addition, we performed follow-up observations of the FRB 20210410D source using the ultra-wideband low (UWL) receiver at the 64-m Murriyang (formerly known as Parkes) radio telescope. The observations spanned a bandwidth of 0.7–4 GHz and were centred at 2368 MHz. We observed the FRB source for a total of 1.9 h on 2022 January 29 and 1.1 h on 2022 July 19. We searched the Parkes data for repeat bursts using the GPU-based single-pulse search software HEIMDALL (Barsdell 2012) and utilized the neural-network trained model FETCH (Agarwal et al. 2020) for the classification of candidates. We employed a tiered subband strategy as described in Kumar et al. (2021) to search the wide-band Parkes data in the DM range of 100–1100 pc cm^{-3}. In these searches, we did not find any significant repetition candidate above an S/N of 8. Using the radiometer equation and assuming a nominal burst width of 1 ms, we can constrain the detectable fluence of the repeat bursts. Our search pipeline was sensitive up to $\sim$1 Jy ms, assuming the repeat bursts are narrow-band $\sim$64 MHz and $\lesssim$ 0.15 Jy ms for a burst spanning the entire UWL band.

4.3.3 Deep Space Network

We also observed FRB 20210410D for a total of $\sim$5.7 h over four separate epochs in 2022 (September 3, October 6, October 15, and October 22) with DSS-43, a 70-m diameter dish located at the Deep Space Network's (DSN) complex in Canberra, Australia. These observations were carried out simultaneously at *S* band (centre frequency of 2.3 GHz) and at *X* band (centre frequency of 8.4 GHz). The data were recorded in both left and right circular polarization modes using the resident pulsar backend in filterbank search mode, where channelized power spectral density measurements are recorded with 1 MHz channel spacing and a time resolution of 512 μs. The *S*-band system spans roughly 120 MHz of bandwidth, while the *X*-band system spans a bandwidth of 400 MHz.

The data processing procedures followed the same steps outlined in previous DSN studies of pulsars and FRBs (e.g. Majid et al. 2021). Data sets in each observing band were first corrected for bandpass slope. We excised bad frequency channels corrupted by radio frequency interference (RFI) using PRESTO's RFIFIND package. To remove any long-time-scale temporal variability, we subtracted a 5 s moving average from each data point. Data sets from the two orthogonal polarizations were then summed in quadrature.

The cleaned data were then dedispersed with the nominal DM value of 578.78 pc cm^{-3}. The resulting time series were searched for FRBs using a matched filtering algorithm by convolving individual time series with logarithmically spaced boxcar functions of widths ranging between 1 and 300 times the intrinsic time resolution of the pulsar backend. We did not detect any candidate bursts above a S/N threshold of 7 in either frequency band, corresponding to a flux threshold of 0.33 Jy at *S* band and 0.19 Jy at *X* band for a 1 ms duration burst.

4.4 Constraining the location of the scattering screen

Given the results of the scattering analysis in Section 4.1.2, we attempt to identify the source of the scattering towards FRB 20210410D. We estimate the scattering time-scale from the Milky Way (MW) to be 0.28 μs at 1 GHz using the NE2001 model. The observed scattering time of $29.4^{+2.8}_{-2.7}$ ms at 1 GHz for FRB 20210410D is much too large to arise from the MW. Therefore, using the analytical framework provided in Ocker, Cordes & Chatterjee (2021), we estimate the expected scattering from FRB 20210410D in two cases: (1) the scattering originates in the host galaxy of FRB 20210410D and (2) the scattering originates in an intervening halo of a foreground galaxy. The scattering due to a foreground galaxy depends not only on its DM contribution but also on the geometric leverage effect, which will increase the scattering by several orders of magnitude relative to scattering in the host galaxy. Fig. 6 shows the expected scattering for both cases as a function of the host galaxy DM contribution and an intervening halo DM contribution. Based

Downloaded from https://academic.oup.com/mnras/article/524/2/2064/7207412 by Univ. of California, Santa Cruz user on 21 July 2023

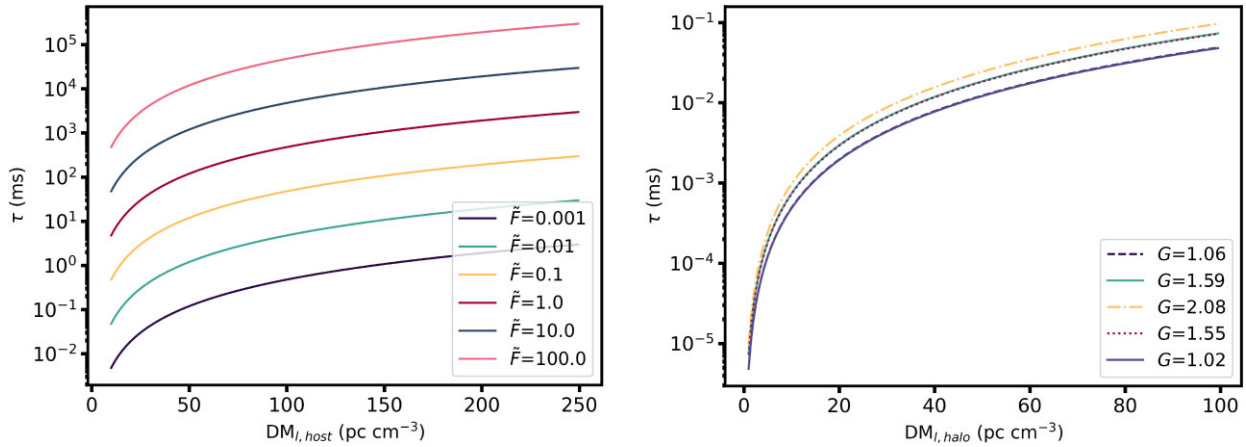

Figure 6. *Left-hand panel*: Scattering time (τ) at 1 GHz as a function of host DM contribution for various values of $\tilde{F}$ that signifies turbulence for FRB 20210410D. *Right-hand panel*: τ at 1 GHz as a function of DM from the halo of an intervening galaxy for values of $G_{\rm scatt}$ (computed from a range of redshifts between 0 and 0.1415) that signifies the geometric boosting to scattering. The analysis is done for a lens with a size of 30 kpc.

on Ocker et al. (2021), the scattering in the host galaxy can be characterized as

$$\tau(\nu, \mathrm{DM}, z) \approx 48.03 \times \frac{A_\tau \tilde{F} G_{\rm scatt}\, \mathrm{DM}_l^2}{(1+z_l)^3\, \nu^4}\ \mu\mathrm{s}, \quad (1)$$

where A_τ is a dimensionless factor approximated to unity, $\tilde{F}$ is the factor that quantifies turbulent density fluctuations in the scattering medium, DM_l is the DM contribution from the scattering screen in either the host galaxy or the intervening halo, z_l is the redshift of the scattering screen, and ν is the observing frequency. $G_{\rm scatt}$ is a factor that quantifies the geometric enhancement of the scattering due to the distance between the source, the scattering screen, and the observer. Following Ocker et al. (2021), we define it as $G_{\rm scatt} \sim d_{\rm sl} d_{\rm lo}/L d_{\rm so}$, where L is the thickness of the thin scattering screen, and $d_{\rm sl}$, $d_{\rm lo}$, and $d_{\rm so}$ are the angular diameter distances of source to lens, lens to observer, and source to observer, respectively. For scattering within the MW or in a distant FRB host galaxy $G_{\rm scatt} = 1$, but $G_{\rm scatt} \gg 1$ for an intervening halo or galaxy.

Similar to Rajwade et al. (2022), we estimate the scattering time for a foreground galaxy at distances ranging from 25 to 75 per cent of the redshift of the host (i.e.) $0.035375 \leq z \leq 0.106125$. For scattering dominated by a screen in the host galaxy, we assume $G \sim 1$ and compute the scattering time for various values of $\tilde{F}$. In the case of scattering dominated by the halo or ISM of an intervening galaxy, we conservatively adopt $\tilde{F} \sim 0.0001$ measured for pulsars in the MW (Ocker et al. 2021) and calculate the scattering times for various values of G derived from the assumed distances to the screen. For this scenario, we also allow $\tilde{F}$ to evolve with redshift according to the cosmic star formation history (SFH) given by using equation 21 in Ocker et al. (2022). According to Ocker et al. (2022), this is based on the assumption that $\tilde{F}$ can evolve with redshift if the underlying turbulence is driven by star formation feedback or gravitational instability.

Chawla et al. (2022) studied the dispersion and scattering properties of a sample of CHIME FRBs and cannot rule out a model of FRBs for which scattering originates in both the local environment and in intervening galaxies. It is apparent from Fig. 6 that the haloes and ISM of intervening galaxies cannot easily account for the scattering time seen in FRB 20210410D (see Table 1) even for all possible values of $G_{\rm scatt}$ within the co-moving distance of the host galaxy of FRB 20210410D. However, the expected τ at 1 GHz can arise from the host galaxy. We thereby conclude that the scattering seen in this FRB originates from the host galaxy.

4.5 Optical follow-up

To identify a host galaxy, we observed the FRB position with the SOAR/Goodman High Throughput Spectrograph in *r* band on 2021 July 19 UT (program ID SOAR2021A-010; PI Fong) and obtained 8×200 s exposures. Four sources were found surrounding the FRB position, as shown in Fig. 5. Further imaging in the *g*, *i*, and *z* band was performed over several nights spanning 2022 August 10–September 03 UT (program ID SOAR2022B-007; PI Gordon), also using 8×200 s exposures in each band. The data were reduced using the PHOTPIPE pipeline (Rest et al. 2005). Each image frame was corrected for bias and flat-fielding following standard procedures using calibration frames obtained on the same night and instrumental configuration. We then registered the calibrated frames using *Gaia* DR3 astrometric standards (Gaia Collaboration 2020) observed in the same field as FRB 20210410D. We performed point spread function (PSF) photometry on point sources in each image using a custom version of DOPHOT (Schechter, Mateo & Saha 1993) and calibrated the photometry with SkyMapper DR2 *griz* standard stars (Onken et al. 2019). Finally, the individual frames for each band were sky-subtracted, stacked, and regridded to a common field centre and pixel scale with SWARP (Bertin 2010) using an optimal median weighting derived from the zero-point in each frame.

To further fill out the spectral energy distribution, we obtained archival imaging of the field of FRB 20210410D from the VISTA Hemisphere Survey (VHS; McMahon et al. 2013) in *Y* and *J* band. We used a custom implementation of SWARP (Bertin 2010) to stack the reduced data, normalizing them to a zero-point of 27.5 AB magnitude. We then performed photometry using the same method as described above.

4.5.1 *PATH analysis*

We performed a Probabilistic Association of Transients to their Hosts (PATH; Aggarwal et al. 2021) analysis to estimate posterior probabilities for the host galaxy candidates of FRB 20210410D. Our analysis adopts the revised priors for FRBs (Shannon et al., in preparation), specifically with an exponential scale length of 1/2

Downloaded from https://academic.oup.com/mnras/article/524/2/2064/7207412 by Univ. of California, Santa Cruz user on 21 July 2023

Table 3. FRB PATH associations.

Name	RA_{cand} (deg)	Dec_{cand} (deg)	θ (arcsec)	ϕ (arcsec)	mag	$P(O)$	$P(O\|x)$
J214420.69−791904.8	326.0862	−79.3180	0.78	0.83	21.78	0.1611	0.9957
Source 1	326.0793	−79.3180	4.69	0.94	20.36	0.6315	0.0043
Source 2	326.0948	−79.3184	5.74	0.50	22.79	0.0657	0.0000
Source 3	326.0786	−79.3187	5.39	0.68	21.92	0.1417	0.0000

the effective radius. Furthermore, we focused the analysis on the SOAR/Goodman *r*-band image. Assuming an unseen prior of $P(U) = 0$, i.e. the host is detected in our relatively deep image, we calculate the posterior probabilities listed in Table 3. It is evident that the galaxy J214420.69−791904.8 which lies closest to the FRB has a very high posterior probability ($P(O) > 99.5$ per cent). We therefore assign it as the host with high confidence. The offset of FRB 20210410D's position from the galaxy core is not uncommon, as in most cases the FRB localizations are significantly offset from the host galaxy centres (Bhandari et al. 2022b).

4.5.2 *Spectroscopic redshift*

We performed longslit spectroscopy with the Gemini-South GMOS spectrograph (Hook et al. 2004; Gimeno et al. 2016) towards FRB 20210410D as part of programs GS-2021B-Q-138 and GS-2022A-Q-143 (PI Tejos). Given the relative positions of the sources of interest, we used the 1 arcsec slit with two position angles (PAs). On UT 2021 October 14, we used a PA = 102 deg covering the FRB host, Source 3 and the (north-western) outskirts of Source 1, and obtained 3 × 1000 s exposures using the R400 grating centred at 700 nm. On UT 2022 June 07, we used a PA = 10 deg covering the centres of Source 1 and Source 2 and obtained 4 × 600 s exposures using the R400 grating centred at 700 and 750 nm (two exposures each).[6] A 2 × 2 binning was used in all the exposures.

We reduced these data with the PYPEIT pipeline (Prochaska et al. 2020) using standard recipes. For the host galaxy, we established a secure redshift of $z = 0.1415$ from several emission lines present in the spectrum (Hα, Hβ, [N II], S II). For Source 1, we could only identify a single emission line and thus the redshift is not secure; given its observed wavelength we deem this line to be Hα at $z = 0.4$ (background). For Sources 2 and 3, we could not identify any strong emission line. We note that Source 3 appears spatially unresolved and thus it may well be a star.

These results have been recently confirmed by subsequent VLT/MUSE integral field unit (IFU) observations obtained on UT 2022 October 25 (e.g. Bernales et al., in preparation), which securely confirm the Hα identification of Source 1 (and thus its redshift); furthermore, these data have securely established that Source 2 is also background to J214420.69−791904.8.

4.5.3 *Spectral energy distribution analysis*

To understand the stellar population properties of the host galaxy J214420.69−791904.8, we used the Bayesian inference code PROSPECTOR (Johnson et al. 2021) with a `continuity` non-parametric SFH (Leja et al. 2019). PROSPECTOR performs stellar population synthesis by jointly fitting photometric and spectroscopic data using the PYTHON-FSPS stellar population synthesis library (Conroy, Gunn & White 2009; Conroy & Gunn 2010). The models were then sampled using the dynamic nested sampling routine DYNESTY (Speagle 2020). Additionally, we implement the Kroupa (2001) initial mass function, Kriek & Conroy (2013) dust attenuation curve, the Gallazzi et al. (2005) mass–metallicity relationship, and a ratio on dust attenuation from young and old stars. To model the spectroscopy, we use a 12th-order Chebyshev polynomial to fit the observed spectrum to the model spectrum. Further, spectroscopic priors include a spectral smoothing parameter, a pixel outlier model to marginalize over noise, and a noise inflation model to ensure a good fit between the observed and model spectrum. Several selected stellar population parameters are presented in Table 1.

[6]The use of two central wavelengths was needed in order to cover a CCD gap produced by a reported failure in one of the GMOS-South CCD amplifiers.

4.6 Disentangling the DM contributions

The total observed DM can be separated into contributions from three primary components,

$$\begin{aligned} \mathrm{DM_{obs}} &= \mathrm{DM_{ISM}} + \mathrm{DM_{halo}} + DM_{EG} \\ \mathrm{DM_{EG}} &= \mathrm{DM_{cosmic}} + \frac{DM_{host}}{1+z} \end{aligned} \tag{2}$$

where $\mathrm{DM_{ISM}}$ is the contribution from the MW's ISM and $\mathrm{DM_{halo}}$ is the contribution from the MW halo. $\mathrm{DM_{EG}}$ is the extragalactic DM contribution composed of $\mathrm{DM_{cosmic}}$ which is the contribution from the cosmic web (combined effects of the intergalactic medium, IGM, and intervening galaxies), and $\frac{\mathrm{DM_{host}}}{1+z}$ which is the redshifted contribution from the host galaxy's ISM including its halo and any gas in the immediate vicinity of the FRB source. We take $\mathrm{DM_{ISM}} = 49.2\ \mathrm{pc\,cm^{-3}}$ to be the average of the estimates from the NE2001 and YMW16 Galactic electron density models. For the MW halo contribution, we use Prochaska & Zheng (2019) to estimate a value of $\sim$40 $\mathrm{pc\,cm^{-3}}$along the line of sight to FRB 20210410D. For $\mathrm{DM_{cosmic}}$, we use the Macquart relation (see Fig. 7) to estimate the mean value given by

$$\langle \mathrm{DM_{cosmic}} \rangle = \int_0^z \frac{c\bar{n}_e(z')\,dz'}{H_0(1+z')^2 \mathrm{E}(z)}, \tag{3}$$

$$\text{where } \mathrm{E}(z) = \sqrt{\Omega_M(1+z')^3 + \Omega_\Lambda}. \tag{4}$$

$\bar{n}_e$ is the mean density of electrons given by

$$\bar{n}_e = f_d(z)\rho_b(z)m_p^{-1}\chi_e \tag{5}$$

$$= f_d(z)\rho_b(z)m_p^{-1}(1 - \mathrm{Y_{He}}/2), \tag{6}$$

in which m_p is the mass of a proton, $f_\mathrm{d}(z)$ is the fraction of cosmic baryons in diffuse ionized gas, and ρ_b is the mass density of baryons defined as

$$\rho_b(z) = \Omega_b \rho_{c,0}(1+z)^3 \tag{7}$$

Downloaded from https://academic.oup.com/mnras/article/524/2/2064/7207412 by Univ. of California, Santa Cruz user on 21 July 2023

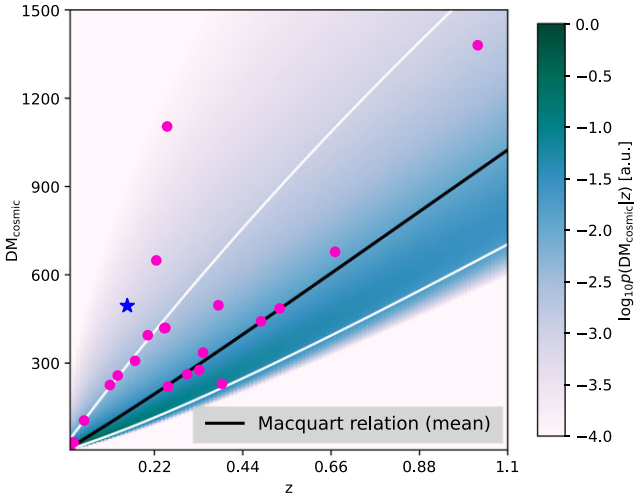

Figure 7. The Macquart relation for a sample of localized FRBs. DM_{cosmic} (after accounting for the MW ISM and 50 pc cm^{-3} for an MW halo contribution) is plotted as a function of the measured redshift for all current arcsecond- and subarcsecond-localized FRBs. The mean denotes the expected relation between DM_{cosmic} and redshift for a Universe based on the Planck cosmology. The white solid lines encompass 90 per cent of the DM_{cosmic} values from a model for ejective feedback in Galactic haloes that is motivated by simulations with feedback parameter $F = 0.32$. FRBs with significant host and/or local DM contributions are seen to deviate significantly from the scatter around the relation. FRB 20210410D with the MW ISM and MW halo DM contributions accounted for is denoted by the star.

where $\rho_{c,0}$ is the critical density and Ω_b is the baryon density parameter. $\chi_e = Y_H + Y_{He}/2 \approx 1 - Y_{He}/2$ is calculated from the primordial hydrogen and helium mass fractions Y_H and Y_{He}.

Using the algorithm encoded in the FRB repository (Prochaska et al. 2019) and the Planck2018 cosmology (Planck Collaboration VI 2020), we obtain $DM_{cosmic} = 121$ pc cm^{-3}. We combine the DM_{ISM}, DM_{halo}, and DM_{cosmic} estimates with the total observed DM to constrain the host galaxy DM to be, $\frac{DM_{host}}{1+z} = 361.4$ pc cm^{-3}.

There is, however, considerable scatter expected in DM_{cosmic} originating from anisotropies in the cosmic web (McQuinn 2014). Adopting the formalism introduced by Macquart et al. (2020), which describes scatter in DM_{cosmic} with the F parameter, and also their estimate of 0.32 for F, the 95 per cent interval on DM_{cosmic} is $DM_{cosmic} = [61, 346]$ pc cm^{-3}. This yields a 95 per cent c.l. range for $\frac{DM_{host}}{1+z} = [140, 425]$ pc cm^{-3}. This is fully consistent with the recent estimate for DM_{host} from James et al. (2022b) who modelled a population of FRBs including 16 with redshift estimates.

4.6.1 *Constraining DM_{host} from* H α *measurements*

The DM contribution of the host galaxy may be independently estimated from its Hα emission by converting the Hα flux density, $F_{H\alpha} = 1.5 \times 10^{-16}$ erg s^{-1} cm^{-2} to a Hα surface brightness in the source frame of $S(H\alpha)_s = 4.65 \times 10^{-16}$ erg s^{-1} cm^{-2} arcsec^{-2} assuming an angular size $\phi = 0.5''$. This $S(H\alpha)_s$ has been obtained by correcting the flux by Galactic extinction and surface brightness dimming. For a temperature $T = 10^4\ T_4$ K, we express the emission measure (EM $= \int n_e^2\, dl$) in the source frame as,

$$\mathrm{EM}(H\alpha)_s = 2.75\, T_4^{0.9} \left[\frac{S(H\alpha)_s}{\mathrm{Rayleigh}}\right] \mathrm{pc\,cm^{-6}} \approx 224.7\,\mathrm{pc\,cm^{-6}}. \quad (8)$$

The host DM in the source frame derived from EM (Cordes et al. 2016; Tendulkar et al. 2017) is given by

$$\mathrm{DM_{host,s}} = 387\,\mathrm{pc\,cm^{-3}}\, L_{kpc}^{1/2} \left[\frac{4f_f}{\zeta(1+\epsilon^2)}\right]^{1/2} \times \left(\frac{\mathrm{EM}(H\alpha)_s}{600\,\mathrm{pc\,cm^{-6}}}\right)^{1/2} \approx 236.8\,\mathrm{pc\,cm^{-3}}, \quad (9)$$

where $\zeta \geq 1$ quantifies cloud-to-cloud variations in the ionized region of depth $L_{kpc}^{1/2}$, with f_f being the volume filling factor of the ionized clouds. $\epsilon \leq 1$ is the fractional density variance inside discrete H II clouds (Cordes et al. 2016; Tendulkar et al. 2017). We estimate the DM_{host} in the observer frame to be 207.5 pc cm^{-3}. Combining the host galaxy DM constraints of 361.4 pc cm^{-3} obtained after accounting for various other DM contributions in Section 4.6, and 207.5 pc cm^{-3} from Hα emission, we estimate that $\approx$154 pc cm^{-3} is unaccounted for. However, this excess is consistent within the 95 per cent c.l. range for $\frac{DM_{host}}{1+z}$ in Section 4.6.1 suggesting that it could well arise from the ISM of the host galaxy.

5 DISCUSSION

5.1 Non-detection of a PRS

Our radio observations do not detect the presence of a PRS, suggestive of a nebula, at the position of FRB 20210410D. Consequently, we place a 3σ upper limit of 6.3×10^{27} erg s^{-1} Hz^{-1} on the luminosity at 1.284 GHz, which is nearly two orders of magnitude below the 1.77 GHz luminosity of the PRS associated with FRB 20121102A (Marcote et al. 2017). If FRB 20210410D is a repeater, it may be much older with an underluminous PRS compared to the more active repeaters like FRB 20121102A (Marcote et al. 2017) and FRB 20190520B (Marcote et al. 2020) which are associated with compact PRSs, or it may be residing in a comparatively more diffuse environment like the repeaters FRB 20200120E (Kirsten et al. 2022) and FRB 20201124A (Ravi et al. 2022), both of which lack a detectable PRS.

5.2 Host galaxy association and properties

We present the PROSPECTOR-normalized spectrum for the host of FRB 20210410D in Fig. 8 and in Table 1 we summarize its key properties. The host galaxy is best described by a stellar mass of $\log(M_*/M_\odot) = 9.46^{+0.05}_{-0.06}$, slightly lower than that of the MW, but not low enough to be considered a dwarf galaxy. The present-day star formation rate of $0.03^{+0.03}_{-0.01}\,M_\odot\,yr^{-1}$ is low, indicating very little active star formation. Further details on the SFH and specific prior ranges can be found in Gordon et al. (2023). We detect Hβ emission, the [N II] doublet, and the [S II] doublet. There is a notable lack of [O III] lines, which is a common feature in FRB host galaxies. Otherwise, the spectrum is typical of an FRB host galaxy (Gordon et al. 2023).

5.3 Host galaxy DM contribution

We consider different possible scenarios for the origin of the host galaxy DM. It could arise from (1) gas in the circumburst region of the progenitor, (2) the ISM of the host galaxy, or (3) gas in an intervening foreground halo. The absence of a PRS and strong Faraday rotation in FRB 20210410D differs from other FRBs which exhibit significant host DMs (Niu et al. 2022), indicating that it is not associated with a complex and highly dynamic magneto-ionic plasma. This is the first FRB that is not associated with a

Downloaded from https://academic.oup.com/mnras/article/524/2/2064/7207412 by Univ. of California, Santa Cruz user on 21 July 2023

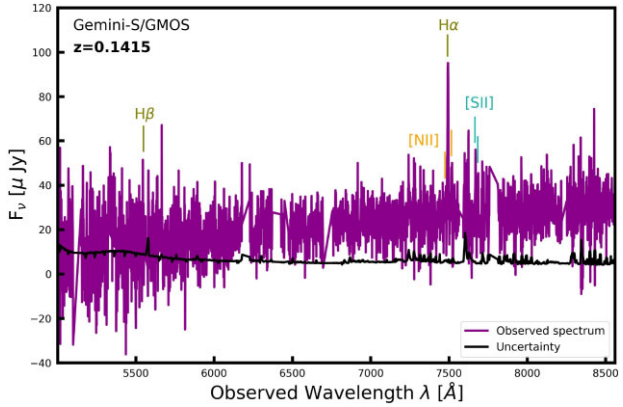

Figure 8. PROSPECTOR-normalized spectrum (see Gordon et al. 2023, for details on the normalization) of FRB 20210410D. Notable emission lines are denoted by coloured lines: Balmer lines in green, nitrogen lines in yellow, and silicon lines in blue.

dwarf galaxy to exhibit a significant host galaxy DM contribution (Tendulkar et al. 2017; Niu et al. 2022; Bhandari et al. 2022a), and seen to deviate beyond the 90 per cent c.l. of the Macquart relation (Macquart et al. 2020) as shown in Fig. 7. It is likely that the host galaxy DM contribution we observe for FRB 20210410D arises from the ISM of the host galaxy rather than the immediate environment or circumburst medium of the progenitor (Feng et al. 2022). This is consistent with the observed large scattering time-scale, which is expected to arise from a scattering screen located in the host galaxy. As the morphology of the galaxy remains unclear, it is impossible to determine if it is an edge-on system. In any case, it is plausible that the FRB sightline passed through high-density clumps of gas, like H II regions in the ISM of the host which could contribute to the host galaxy DM.

5.4 Photometric redshifts

We estimated photometric redshifts, $z_{\rm phot}$, for the sources in Fig. 5 using the EAZY template fitting code (Brammer, van Dokkum & Coppi 2008). We fit flux measurements in the SOAR *griz* and VISTA *YJ* bands with the `CWW + KIN` set while allowing superpositions of the individual templates. Although VISTA *Ks* band data were available, we excluded them from the fits as those fluxes appeared to be consistently ∼2 times higher than the expected value from the template fits. The photometric redshifts thus obtained are listed in Table 4. An example fit is shown in Fig. 9. We note that the host $z_{\rm phot}$ is not entirely consistent with the secure spectroscopic redshift. In general, this, along with the wide photometric redshift error margins for all sources in the field imply the need for flux measurements in more bands if not spectroscopic observations of all sources for more accurate redshifts.

5.5 Pulse morphology

It can be seen in Fig. 2, that our pulse profile model seems to require a shifted low frequency emission region, which suggests a subpulse scenario. This time-frequency downward drifting structure seen in FRB 20210410D is suggestive of a repeater origin when compared against the large sample of FRBs in Pleunis et al. (2021b).

In a pulse profile, the effect of thin-screen scattering appears as a truncated exponential or 'exponential tail', which is a broadening of the trailing edge (or 'tail') of the profile (Lyne & Thorne 1975). The scattering measured for this FRB shows that it is dominated by the scattering contribution from the host galaxy (see Section 4.1.2). This is further highlighted if we study the correlation between the host contribution to the DM and the total amount of scattering. Fig. 10 compares the scattering time as a function of DM for pulsars in the MW with that of FRB 20210410D. It is clear that for the host contribution to the total DM, the scattering time-scale is consistent with what one would obtain for an object in our Galaxy (Bhat et al. 2004; Lewandowski, Kowalińska & Kijak 2015). This shows that the turbulent environment in the host galaxy is similar to that observed in the plane of our own Galaxy.

Table 4. EAZY photometric redshifts of sources.

Name	$z_{\rm phot}$	68 per cent c.i.	95 per cent c.i.
J214420.69−791904.8	0.44	0.41–0.50	0.22–0.54
Source 1	0.47	0.45–0.52	0.20–0.59
Source 2	0.58	0.53–0.64	0.50–0.65
Source 3	0.53	0.44–0.63	0.21–0.68

6 SUMMARY

We present the discovery and subarcsec localization of FRB 20210410D with the MeerKAT radio telescope. FRB 20210410D is the first one to exhibit a $\rm DM_{cosmic}$ which deviates from the Macquart relation while not being associated with a dwarf galaxy. The host galaxy mass is only slightly lower than that of the MW. While the potential downward frequency drifting in the spectrum is reminiscent of repeaters (Pleunis et al. 2021b), we are yet to detect a repeat pulse from this source. Based on the absence of a PRS, we place a 3σ upper limit of 6.3×10^{27} erg s^{-1} Hz^{-1} on the luminosity at 1.284 GHz. We investigated the origin of the observed scattering in FRB 20210410D and find that it cannot originate from a screen in the MW or the halo of an intervening galaxy. Additionally, the lack of a PRS associated with the FRB means that the scattering is most likely dominated by turbulent material in the ISM of the host galaxy. The absence of strong Faraday rotation in FRB 20210410D sets it apart from other FRBs with large values of $\rm DM_{cosmic}$. We encourage follow-up observations to search for repeating pulses.

ACKNOWLEDGEMENTS

MC would like to thank Clancy W. James for help with the ZDM code. The authors would also like to thank the South African Radio Astronomy Observatory staff for their help with scheduling the observations. MC, BWS, KMR, TB, LND, SS, MM, VM, MS, and FJ acknowledge funding from the European Research Council (ERC) under the European Union's Horizon 2020 research and innovation programme (grant agreement no. 694745). MC acknowledges support of an Australian Research Council Discovery Early Career Research Award (project number DE220100819) funded by the Australian Government and the Australian Research Council Centre of Excellence for All Sky Astrophysics in 3 Dimensions (ASTRO 3D), through project number CE170100013. KMR acknowledges support from the Vici research program 'ARGO' with project number 639.043.815, financed by the Dutch Research Council (NWO). WF, CK, JXP, ACG, SS, and NT as members of the Fast and Fortunate for FRB follow-up team acknowledge support from NSF grants AST-1911140 and AST-1910471. NT and LB acknowledge support by FONDECYT grant 11191217. The MeerKAT telescope

Downloaded from https://academic.oup.com/mnras/article/524/2/2064/7207412 by Univ. of California, Santa Cruz user on 21 July 2023

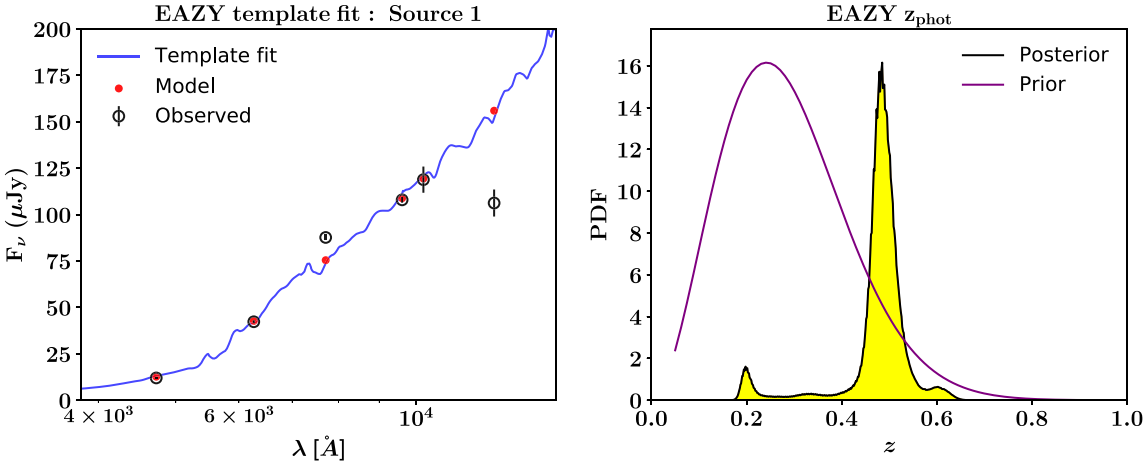

Figure 9. An example photometric redshift estimation for Source 1 using EAZY. *Left*: Best-fitting template spectrum (blue) with input photometry (black) overlaid. The red points show synthetic photometry from the best-fitting template. *Right*: The resultant z_{phot} probability distribution function (PDF). The broad, multimodal posterior distribution implies more data points are necessary to better constrain the galaxy spectrum better. This is the case for all sources analysed (see Table 4 for a summary).

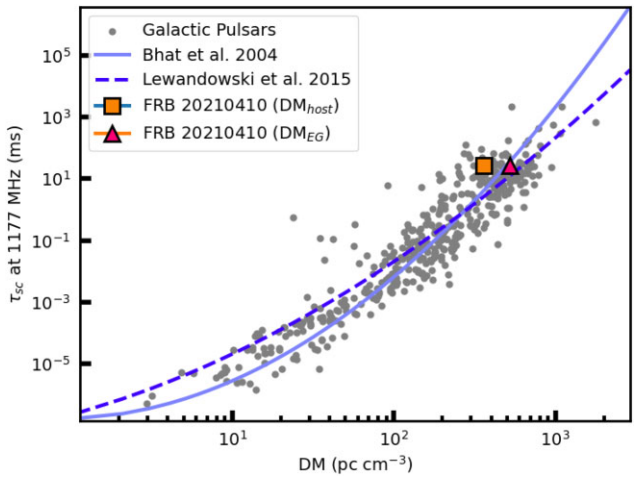

Figure 10. DM as a function of pulse scattering time-scale for pulsars in the Galaxy. The extragalactic and the host DM contributions to FRB 20210410D are marked with a triangle and a square. The solid line corresponds to the best-fitting relation between scattering and DM from the Galactic pulsars as presented in Bhat et al. (2004) while the dashed line is the best fit from Lewandowski et al. (2015).

is operated by the South African Radio Astronomy Observatory (SARAO), which is a facility of the National Research Foundation, an agency of the Department of Science and Innovation. The Parkes Radio Telescope (Murriyang) is managed by CSIRO. The FBFUSE beamforming cluster was funded, installed, and operated by the Max-Planck-Institut für Radioastronomie and the Max-Planck-Gesellschaft. We acknowledge the Wiradjuri people as the traditional owners of the Parkes observatory site. We acknowledge the use of the ilifu cloud computing facility – http://www.ilifu.ac.za, a partnership between the University of Cape Town, the University of the Western Cape, the University of Stellenbosch, Sol Plaatje University, the Cape Peninsula University of Technology, and the South African Radio Astronomy Observatory. The ilifu facility is supported by contributions from the Inter-University Institute for Data Intensive Astronomy (IDIA – a partnership between the University of Cape Town, the University of Pretoria and the University of the Western Cape), the Computational Biology division at UCT, and the Data Intensive Research Initiative of South Africa (DIRISA).

Based on observations obtained at the international Gemini Observatory, a programme of NSF's NOIRLab, which is managed by the Association of Universities for Research in Astronomy (AURA) under a cooperative agreement with the National Science Foundation on behalf of the Gemini Observatory partnership: the National Science Foundation (United States), National Research Council (Canada), Agencia Nacional de Investigación y Desarrollo (Chile), Ministerio de Ciencia, Tecnología e Innovación (Argentina), Ministério da Ciência, Tecnologia, Inovações e Comunicações (Brazil), and Korea Astronomy and Space Science Institute (Republic of Korea). The Gemini data were obtained from programs GS-2021B-Q-138 and GS-2022A-Q-143 (PI Tejos), and were processed with PYPEIT (Prochaska et al. 2020).

Based in part on observations obtained at the Southern Astrophysical Research (SOAR) telescope, which is a joint project of the Ministério da Ciência, Tecnologia e Inovações (MCTI/LNA) do Brasil, the US National Science Foundation's NOIRLab, the University of North Carolina at Chapel Hill (UNC), and Michigan State University (MSU).

Based on observations obtained as part of the VISTA Hemisphere Survey, ESO Progam, 179.A-2010 (PI: McMahon)

A portion of this research was performed at the Jet Propulsion Laboratory, California Institute of Technology, under a Research and Technology Development Grant through a contract with the National Aeronautics and Space Administration. U.S. government sponsorship is acknowledged.

DATA AVAILABILITY

The data will be made available upon reasonable request to the authors.

REFERENCES

Adámek K., Armour W., 2020, ApJS, 247, 56
Agarwal D., Aggarwal K., Burke-Spolaor S., Lorimer D. R., Garver-Daniels N., 2020, MNRAS, 497, 1661

Downloaded from https://academic.oup.com/mnras/article/524/2/2064/7207412 by Univ. of California, Santa Cruz user on 21 July 2023

Aggarwal K., Budavári T., Deller A. T., Eftekhari T., James C. W., Prochaska J. X., Tendulkar S. P., 2021, ApJ, 911, 95
Armour W. et al., 2012, in Ballester P., Egret D., Lorente N. P. F., eds, ASP Conf. Ser. Vol. 461, Astronomical Data Analysis Software and Systems XXI. Astron. Soc. Pac., San Francisco, p. 33
Bannister K. W. et al., 2019, Science, 365, 565
Barr E. D., 2018, in Weltevrede P., Perera B. B. P., Preston L. L., Sanidas S., eds, Proc. IAU Symp. 337, Pulsar Astrophysics the Next Fifty Years. Kluwer, Dordrecht, p. 175
Barsdell B. R., 2012, PhD thesis, Swinburne University of Technology
Bertin E., 2010, Astrophysics Source Code Library, record ascl:1010.068
Bhandari S. et al., 2022a, ApJ, 948, 11
Bhandari S. et al., 2022b, AJ, 163, 69
Bhat N. D. R., Cordes J. M., Camilo F., Nice D. J., Lorimer D. R., 2004, ApJ, 605, 759
Brammer G. B., van Dokkum P. G., Coppi P., 2008, ApJ, 686, 1503
Caleb M., Spitler L. G., Stappers B. W., 2018, Nat. Astron., 2, 839
Caleb M. et al., 2022, Nat. Astron., 6, 828
Chatterjee S. et al., 2017, Nature, 541, 58
Chawla P. et al., 2022, ApJ, 927, 35
Chen W., Barr E., Karuppusamy R., Kramer M., Stappers B., 2021, Journal of Astronomical Instrumentation, 10, 178
Chibueze J. O. et al., 2022, MNRAS, 515, 1365
Connor L. et al., 2023, ApJ, 949, L26
Conroy C., Gunn J. E., 2010, ApJ, 712, 833
Conroy C., Gunn J. E., White M., 2009, ApJ, 699, 486
Cordes J. M., Wharton R. S., Spitler L. G., Chatterjee S., Wasserman I., 2016, preprint (arXiv:1605.05890)
Day C. K. et al., 2020, MNRAS, 497, 3335
Driessen L. N. et al., 2022, MNRAS, 512, 5037
Feng Y. et al., 2022, Science, 375, 1266
Gaia Collaboration, 2020, A&A, 649, 35
Gajjar V. et al., 2018, ApJ, 863, 2
Gallazzi A., Charlot S., Brinchmann J., White S. D. M., Tremonti C. A., 2005, MNRAS, 362, 41
Gimeno G. et al., 2016, in Evans C. J., Simard L., Takami H., eds, Proc. SPIE Conf. Ser. Vol. 9908, Ground-based and Airborne Instrumentation for Astronomy VI. SPIE, Bellingham, p. 99082S
Gordon A. C. et al., 2023, The Demographics, Stellar Populations, and Star Formation Histories of Fast Radio Burst Host Galaxies: Implications for the Progenitors
Hessels J. W. T. et al., 2019, ApJ, 876, L23
Hook I. M., Jørgensen I., Allington-Smith J. R., Davies R. L., Metcalfe N., Murowinski R. G., Crampton D., 2004, PASP, 116, 425
James C. W., Prochaska J. X., Macquart J. P., North-Hickey F. O., Bannister K. W., Dunning A., 2022a, MNRAS, 509, 4775
James C. W. et al., 2022b, MNRAS, 516, 4862
Jankowski F., Bezuidenhout M. C. et al., 2023, MNRAS, 1, 1
Johnson B. D., Leja J., Conroy C., Speagle J. S., 2021, ApJS, 254, 22
Kirsten F. et al., 2022, Nature, 602, 585
Kriek M., Conroy C., 2013, ApJ, 775, L16
Kroupa P., 2001, MNRAS, 322, 231
Kumar P. et al., 2021, MNRAS, 500, 2525
Leja J., Carnall A. C., Johnson B. D., Conroy C., Speagle J. S., 2019, ApJ, 876, 3
Lewandowski W., Kowalińska M., Kijak J., 2015, MNRAS, 449, 1570
Luo R., Men Y., Lee K., Wang W., Lorimer D. R., Zhang B., 2020, MNRAS, 494, 665
Lyne A. G., Thorne D. J., 1975, MNRAS, 172, 97
McConnell D., Sadler E. M., Murphy T., Ekers R. D., 2012, MNRAS, 422, 1527
McMahon R. G., Banerji M., Gonzalez E., Koposov S. E., Bejar V. J., Lodieu N., Rebolo R., VHS Collaboration, 2013, Messenger, 154, 35
Macquart J. P. et al., 2020, Nature, 581, 391
McQuinn M., 2014, ApJ, 780, L33
Majid W. A. et al., 2021, ApJ, 919, L6
Mannings A. G. et al., 2021, ApJ, 917, 75
Mannings A. G. et al., 2022, preprint (arXiv:2209.15113)
Marcote B. et al., 2017, ApJ, 834, L8
Marcote B. et al., 2020, Nature, 577, 190
Niu C. H. et al., 2022, Nature, 606, 873
Ocker S. K., Cordes J. M., Chatterjee S., 2021, ApJ, 911, 102
Ocker S. K., Cordes J. M., Chatterjee S., Gorsuch M. R., 2022, ApJ, 934, 71
Onken C. A. et al., 2019, Publ. Astron. Soc. Aust., 36, e033
Parent E. et al., 2020, ApJ, 904, 92
Planck Collaboration VI, 2020, A&A, 641, A6
Platts E., Weltman A., Walters A., Tendulkar S. P., Gordin J. E. B., Kandhai S., 2019, Phys. Rep., 821, 1
Pleunis Z. et al., 2021a, ApJ, 911, L3
Pleunis Z. et al., 2021b, ApJ, 923, 1
Prochaska J. X., Zheng Y., 2019, MNRAS, 485, 648
Prochaska J. X., Simha S., Law C., Tejos N., mneeleman, 2019, FRBs/FRB: First DOI Release of This Repository
Prochaska J. X. et al., 2020, J. Open Source Softw., 5, 2308
Qiu H. et al., 2020, MNRAS, 497, 1382
Rafiei-Ravandi M. et al., 2021, ApJ, 922, 42
Rajwade K. et al., 2020, Proceedings of the SPIE, 11447, 8
Rajwade K. M. et al., 2022, MNRAS, 514, 1961
Ravi V. et al., 2022, MNRAS, 513, 982
Rest A. et al., 2005, ApJ, 634, 1103
Ryder S. D. et al., 2022, preprint (arXiv:2210.04680)
Schechter P. L., Mateo M., Saha A., 1993, PASP, 105, 1342
Seymour A., Michilli D., Pleunis Z., 2019, Astrophysics Source Code Library, record ascl:1910.004
Speagle J. S., 2020, MNRAS, 493, 3132
Tendulkar S. P. et al., 2017, ApJ, 834, L7

[1]*Sydney Institute for Astronomy, School of Physics, The University of Sydney, NSW 2006, Australia*
[2]*Jodrell Bank Centre for Astrophysics, University of Manchester, Oxford Road, Manchester M13 9PL, UK*
[3]*ASTRO3D: ARC Centre of Excellence for All-sky Astrophysics in 3D, ACT 2601, Australia*
[4]*CSIRO, Space and Astronomy, PO Box 1130, Bentley, WA 6102, Australia*
[5]*Center for Interdisciplinary Exploration and Research in Astrophysics (CIERA) and Department of Physics and Astronomy, Northwestern University, Evanston, IL 60208, USA*
[6]*Instituto de Física, Pontificia Universidad Católica de Valparaíso, Casilla 4059, Valparaíso, Chile*
[7]*SKA Observatory, Jodrell Bank, Lower Withington, Macclesfield SK119FT, UK*
[8]*Centre for Space Research, North-West University, Potchefstroom Campus, Private Bag X6001, Potchefstroom 2520, South Africa*
[9]*Department of Mathematical Sciences, University of South Africa, Cnr Christian de Wet Rd and Pioneer Avenue, Florida Park 1709, Roodepoort, South Africa*
[10]*Department of Physics and Astronomy, Faculty of Physical Sciences, University of Nigeria, Carver Building, 1 University Road, Nsukka 410001, Nigeria*
[11]*ASTRON, the Netherlands Institute for Radio Astronomy, Oude Hoogeveensedijk 4, NL-7991 PD Dwingeloo, the Netherlands*
[12]*INAF-Osservatorio Astrofisico di Catania, Via S. Sofia 78, I-95123 Catania, Italy*
[13]*Inter-University Institute for Data Intensive Astronomy & Department of Astronomy, University of Cape Town, Private Bag X3, Rondebosch 7701, South Africa*
[14]*CSIRO, Space and Astronomy, PO Box 76, Epping, NSW 1710, Australia*
[15]*ARC Centre of Excellence for Gravitational Wave Discovery (OzGrav), PO Box 218, Hawthorn, VIC 3122, Australia*
[16]*Centre for Astrophysics and Supercomputing, Swinburne University of Technology, PO Box 218, Hawthorn, VIC 3122, Australia*
[17]*Department of Particle Physics & Astrophysics, Weizmann Institute of Science, Rehovot 7610001, Israel*

Downloaded from https://academic.oup.com/mnras/article/524/2/2064/7207412 by Univ. of California, Santa Cruz user on 21 July 2023

[18]*Jet Propulsion Laboratory, California Institute of Technology, Pasadena, CA 91109, USA*
[19]*Division of Physics, Mathematics, and Astronomy, California Institute of Technology, Pasadena, CA 91125, USA*
[20]*LPC2E, Université d'Orléans, CNRS, 3A Avenue de la Recherche Scientifique, F-45071 Orléans, France*
[21]*Department of Physics, IISER Bhopal, Bhauri Bypass Road, Bhopal 462066, India*
[22]*Max-Planck-Institut für Radioastronomie, Auf dem Hügel 69, D-53121 Bonn, Germany*
[23]*University of California, Santa Cruz, 1156 High St., Santa Cruz, CA 95064, USA*
[24]*Kavli Institute for the Physics and Mathematics of the Universe, 5-1-5 Kashiwanoha, Kashiwa 277-8583, Japan*
[25]*Department of Physics, Astrophysics, University of Oxford, Denys Wilkinson Building, Keble Road, Oxford OX1 3RH, UK*
[26]*Department of Physics and Electronics, Rhodes University, PO Box 94, Grahamstown 6140, South Africa*
[27]*IRFU, CEA, Université Paris-Saclay, F-91191 Gif-sur-Yvette, France*

This paper has been typeset from a TEX/LATEX file prepared by the author.

Downloaded from https://academic.oup.com/mnras/article/524/2/2064/7207412 by Univ. of California, Santa Cruz user on 21 July 2023

© 2023 The Author(s)
Published by Oxford University Press on behalf of Royal Astronomical Society